Geophysical Research Letters

RESEARCH LETTER
10.1029/2019GL084892

Frequency-Dependent *P* Wave Polarization and Its Subwavelength Near-Surface Depth Sensitivity

Sunyoung Park[1], Victor C. Tsai[2], and Miaki Ishii[3]

[1]Division of Geological and Planetary Sciences, California Institute of Technology, Pasadena, CA, USA, [2]Department of Earth, Environmental and Planetary Sciences, Brown University, Providence, RI, USA, [3]Department of Earth and Planetary Sciences, Harvard University, Cambridge, MA, USA

Key Points:
- The depth sensitivity of P wave polarization peaks at the surface and becomes negligible at a depth that is shallower than its wavelength
- The frequency content and the near-surface shear wave speeds are the main factors that determine the depth sensitivity
- P wave polarization is a useful tool for constraining shallow 1-D structure from about 10 m to several kilometers at 0.1 to 10 Hz

Supporting Information:
- Supporting Information S1

Correspondence to:
S. Park,
sunnyp@caltech.edu

Citation:
Park, S., Tsai, V. C., & Ishii, M. (2019). Frequency-dependent *P* wave polarization and its subwavelength near-surface depth sensitivity. *Geophysical Research Letters*, *46*. https://doi.org/10.1029/2019GL084892

Received 9 AUG 2019
Accepted 8 NOV 2019
Accepted article online 15 NOV 2019

Abstract Near-surface structure is crucial to assessing seismic hazards and understanding earthquakes and surface processes yet is a major challenge to robustly image. Recently, an approach based on body-wave polarization was introduced for constraining shallow seismic structure, but the depth sensitivity of the polarization measurement has remained unclear. Using waveform simulations based on a layer over a half space, we find that the depth sensitivity of *P* wave polarization peaks at the surface and decreases abruptly over a depth range shorter than its wavelength. A strong frequency dependence provides constraints on local 1-D structure, with frequencies between 0.1 and 10 Hz illuminating structure at depths of 10 m to several kilometers. Applying these results to teleseismic recordings in Japan provides constraints on structure at about 120 to 750 m, including a distinctive weak zone along the Median Tectonic Line in the Kii peninsula and Awaji Island.

Plain Language Summary Shallow structure controls the level of ground shaking and hence is critical in assessing seismic hazards. Conventionally, drilling or local seismic surveys are performed to image the near surface, but their high cost has resulted in extremely sparse coverage of studied sites worldwide. Here we demonstrate that the directions of *P* waves that are naturally generated by local or distant earthquakes constrain the structure immediately below the seismometer where the *P* waves are recorded. Our finding suggests that frequency-dependent measurements of *P* wave directions is a promising tool for studying shallow structure that is noninvasive and cost effective. Application to data recorded in Japan reveals structure at about 120- to 750-m depth, including a weak zone along a segment of the Median Tectonic Line.

1. Introduction

Improving our knowledge of near-surface structure, for example, the shallow crust and sedimentary basins, is crucial to numerous areas of earth sciences. Shallow structure in the top tens to hundreds of meters controls the level of ground shaking and, hence, is fundamental to seismic hazard assessment (e.g., Boore et al., 1997; Borcherdt & Glassmoyer, 1992; Shearer & Orcutt, 1987). For the same reason, imaging shallow structure is essential for studying seismic source properties such as radiated energy, stress drop, and rupture dimensions; not accounting for site amplification can result in considerable inaccuracy in the estimates of source parameters (e.g., Abercrombie, 1997). Furthermore, imaging the near surface is important for understanding Earth surface processes including the dynamics of the critical zone (e.g., Parsekian et al., 2015) and for connecting observations at the Earth's surface to tectonics and deeper processes.

Despite the significance of near-surface structure, it has been poorly understood due to various challenges. Most direct approaches like well drilling (e.g., Levander et al., 1994; Wu et al., 1994) or field experiments using explosives or vibroseis (e.g., Choukroune, 1989) are expensive and limited in spatial coverage. Conventional body wave analyses based on travel times are sensitive to structure along the whole ray path through the deeper part of the Earth (e.g., Dahlen et al., 2000; Woodward, 1992), which poses difficulties in imaging the shallow subsurface. Sensitivity of surface-wave group and phase velocities (e.g., Laske & Masters, 1996; Mitchell & Yu, 1980) is bounded near the Earth's surface, but wavelengths are often too long to resolve fine structure near the surface.

Surface-wave polarization or ellipticity has been used to study shallow structure (e.g., Berbellini et al., 2017; Lin et al., 2014; Tanimoto & Rivera, 2008). Similarly, body-wave polarization, that is, the direction of body-wave particle motion measured at the free surface, has been demonstrated to be effective in studying near-

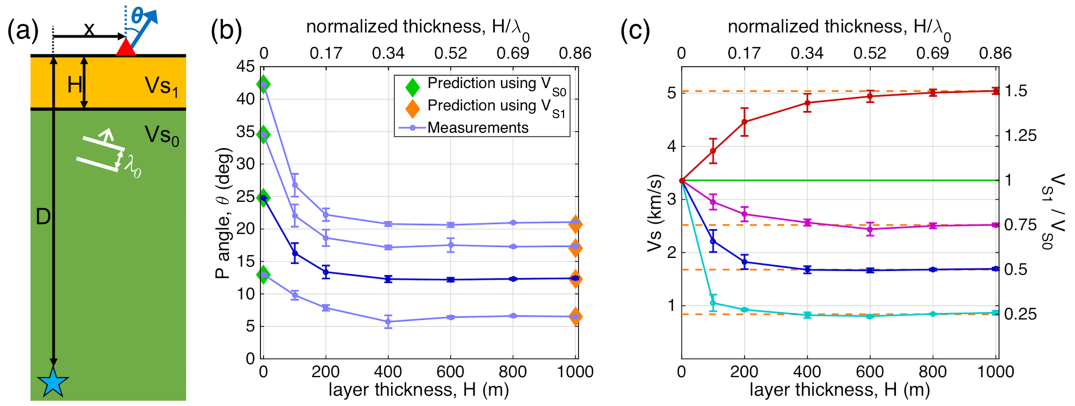

Figure 1. (a) Schematic for the numerical simulation. Source (blue star) is located at depth D, within the background medium with shear wave speed of V_{S1}. A layer with shear wave speed V_{S1} and thickness H overlies the half-space. A P wave with wavelength λ_0 propagates from the source and is recorded by the receiver (red triangle) at the surface located at horizontal distance, x. The synthetic P wave polarization at the receiver is denoted as θ. (b) P wave polarization angles measured for various layer thicknesses for $V_{S1} = 0.5\ V_{S0}$. Each line represents the angles measured at horizontal distances (×) of 20 (bottom; light blue), 40 (second bottom; blue), 60 (third from the bottom; light blue), and 80 km (top; light blue). Measurements are made for $H = 0$, 100, 200, 400, 600, 800, and 1,000 m, which correspond to 0, 0.17, 0.34, 0.52, and 0.86 of the incoming wavelength λ_0. Each circle with its error bar is the polarization measurement and its uncertainty obtained from the synthetic data. Predicted values of the P wave polarization angle based on V_{S0} (green diamond) and V_{S1} (orange diamond) are plotted as the two end members at $H = 0$, and 1,000 m, respectively. (c) Estimated shear wave speeds based on the P wave polarization angles for various layer thickness and wave speed contrasts. Each line corresponds to different V_{S1} of 0.25 (cyan), 0.5 (blue), 0.75 (magenta), and 1.5 (red) times V_{S0} at a fixed horizontal distance of 40 km. The blue line corresponds to the blue line in (b). The solid green line represents the V_{S0} (3.36 km/s), and orange dashed lines represent various V_{S1} (0.25, 0.5, 0.75, and 1.5 times V_{S0}).

surface structure (e.g., Kruger, 1994; Park & Ishii, 2018). Other closely related measurements including horizontal-to-vertical body-wave spectral ratios (e.g., Phinney, 1964) and zero-time receiver function amplitudes (e.g., Hannemann et al., 2016; Svenningsen & Jacobsen, 2007) have also been explored to understand shallow (0.1–10s of kilometer) 1-D structure.

Direct measurements of body-wave polarization can potentially constrain even shallower structure since such measurements do not require processing such as deconvolution which can limit shallow depth sensitivity. In order to understand the utility of direct body-wave polarization measurements for imaging shallow structure, this paper aims to systematically examine their depth sensitivities. We find a strong frequency dependence of polarization measurements, a distinctive characteristic that is not pronounced in body-wave travel-time measurements. Here we focus on P wave polarization which is simpler than S wave polarization in that it is nearly exclusively sensitive to shear structure (Park & Ishii, 2018). Note that the term polarization is sometimes also used to refer to the direction of the ray path (e.g., Hu et al., 1994), which is different from the direction of particle motion measured at the Earth's surface considered throughout this manuscript.

2. Methods for Estimating *P* Wave Polarization Sensitivity

2.1. Model Setup and Simulation

In order to test the depth sensitivity of P wave polarization, we model the P waveform using a layer over a half space (Figure 1a). We assume a background medium with a shear wave speed of V_{S0}=3.36 km/s based on the upper-crustal value from IASP91 (Kennett & Engdahl, 1991). The shallow layer has a thickness H and shear wave speed V_{S1} Unless otherwise noted, the compressional wave speeds are assumed to be $\sqrt{3}$ times the shear wave speeds, that is, a Poisson's ratio of 0.25, and the density is fixed as 2.72 g/cm^3 in both layers (Kennett & Engdahl, 1991).

For the waveform calculation, we use the reflectivity algorithm of Kennett (1986). To investigate the depth sensitivity of P wave polarization for a range of ray parameters, we place multiple receivers at the surface at different horizontal distances from a single source at depth D. We use a Ricker wavelet source with central

frequency . The frequency f is sufficiently high that the wavelength is much shorter than the traveling path lengths, which ensures that the plane wave approximation holds at the surface.

For given medium properties, source-receiver geometry, and input frequency f, we examine how the P wave polarization changes as the depth of the overlying layer H varies. One end-member case is when H is zero, where the polarization is only affected by V_{S0}.. The other is when H is larger than D, where the polarization is only affected by V_{S1}. We aim to understand at which depth the transition between the two cases occurs, and how the transitioning depth compares with the wavelengths. Note that varying H for a fixed f has an identical effect to varying f with a fixed H (see section 3).

2.2. Polarization Measurement and Estimate of Shear Wave Speed

We measure P wave polarization based on principal component analysis (Pearson, 1901). For demeaned vertical and radial time series written as column vectors $\boldsymbol{q} = [q_1, ..., q_N]$ and $\boldsymbol{r} = [r_1, ..., r_N]$, we find the eigenvectors ($\boldsymbol{u_1}$, $\boldsymbol{u_2}$) and eigenvalues (l_1,l_2; $l_1 \geq l_2$) of the covariance matrix,

$$\boldsymbol{C} = \frac{1}{N}\begin{bmatrix} \boldsymbol{q^T q} & \boldsymbol{q^T r} \\ \boldsymbol{r^T q} & \boldsymbol{r^T r} \end{bmatrix}, \tag{1}$$

where T denotes transpose. The angle between the first eigenvector $\boldsymbol{u_1}$ (corresponding to l_1) and the vertical direction is the measured polarization angle θ. Robustness of the polarization measurement is assessed as the fraction of the data variance that is explained by the measured polarization direction, $\frac{l_1}{l_1+l_2}$, that is, the degree of linearity of particle motion. We examine the polarization angle and linearity of the particle motion for gradually increasing time window (i.e., increasing N). For each time series with length N, we estimate the shear wave speed V_S^N for each P-wave polarization measurement θ_N using

$$V_S^N = \frac{sin\left(\frac{\theta_N}{2}\right)}{p} \tag{2}$$

where P is the ray parameter (Svenningsen & Jacobsen, 2007).

When the P wave arrives at the interface between the layer and the half space, it generates P- to S-converted waves which arrive after the direct wave (Figure S1a). As the time window for the principal component analysis increases to include the converted wave, the polarization angle changes slightly (Figure S1b). Since the converted wave has a small amplitude and its particle motion is nearly perpendicular to that of the direct wave, that is, nearly orthogonal to the first principal component, the change in the measured angle caused by the converted wave is limited. Nonetheless, we reduce the variability caused by the converted wave by selecting measurements with nearly 100% linearity, based on the fact that the direct wave has linear particle motion and that the linearity deteriorates when the converted wave arrives. The final estimate of polarization angle θ is determined as the mean of these individual measurements θ_N, and their standard deviation is a measure of the uncertainty. The final estimate and associated uncertainty of shear wave speed V_S^* are also derived from taking the mean and standard deviation of the corresponding set of V_S^N measurements (Figure S1c). Note that multiples, that is, reflected waves within the layer, arrive later than the converted wave and do not have significant effect on the measured polarization.

2.3. Evaluation of Depth Sensitivity of *P* Wave Polarization

Based on the estimated shear wave speed V_S^* for different H, we can evaluate the depth sensitivity of P wave polarization as a function of depth. For a layer over a half space with V_{S1} and V_{S0}, we define the depth sensitivity, $s(z)$, such that it represents the contribution from V_{S1} and V_{S0} to V_S^*, that is,

$$V_S^* = V_{S1}\int_0^H s(z)dz + V_{S0}\int_H^\infty s(z)dz. \tag{3}$$

The depth sensitivity is defined to sum to unity, that is, $\int_0^\infty s(z)dz = 1$, where $\int_H^\infty s(z)dz$ can be rewritten as $1-\int_0^H s(z)dz$. This definition of sensitivity is distinct from that of conventional Fréchet kernels in that it is obtained by changing H for a layer over a half space and is associated with absolute wave speeds instead of perturbations of wave speeds at certain depths. Since near-surface wave speeds can vary drastically at different sites as opposed to the percent-level perturbations typically assumed for mantle tomography

(e.g., Woodward, 1992), we have chosen to consider the depth sensitivity as in equation (3), which allows us to explore a large range of V_{S1} and H. Rearranging equation (3) yields

$$S_1 = \int_0^H s(z)dz = \frac{V_{S0} - V_S^*}{V_{S0} - V_{S1}}, \quad (4)$$

which represents the cumulative sensitivity to the layer, while the cumulative sensitivity to the background medium S_0 is $1 - S_1$. Differentiating equation (4) with H gives

$$s(H) = -\frac{1}{V_{S0} - V_{S1}} \frac{dV_S^*}{dH}. \quad (5)$$

Therefore, the sensitivity for given V_{S1} and V_{S0} can be calculated by measuring how quickly the wave speed estimate V_S^* changes with H relative to the total difference in shear wave speed. For a given depth sensitivity, we estimate $H_{0.5}$ and $H_{0.95}$, which denote the depths that satisfy $\int_0^{H_{0.5}} s(z)dz = 0.5$ and $\int_0^{H_{0.95}} s(z)dz = 0.95$. Determining these two depths allows us to understand the average depth and the depth limit that P wave polarization is sensitive to.

3. Results and Discussion

We have chosen simulation parameters to investigate a broad range of scenarios. For testing different sets of ray parameters, receivers are located at horizontal distances x of 20 to 80 km from the source, while the source is placed at the depth of 100 km, that is, $D = 100$ km (Figure 1a). For a background compressional wave speed of 5.82 km/s ($\sqrt{3}\, V_{S0}$), these source-receiver geometries correspond to ray parameters of about 0.03 to 0.11 s/km or 3.7 to 11.9 s/°. This range includes ray parameters from teleseismic events, that is, from about 4.6 to 8.8 s/° and ones from local or regional sources with incident angles that are steeper or shallower than teleseismic cases. We find that the typical range of ray parameters does not have a significant effect on the depth sensitivity of P wave polarizations (supporting information Text S1 and Figure S2).

We test shear wave speed ratios of V_{S1}/V_{S0}= 0.25, 0.5, and 0.75. Even though V_{S1} is often smaller compared to V_{S0}, we also test a case of a fast layer with $V_{S1} = 1.5\, V_{S0}$ which can occur at some sites, for example, an ice or asphalt layer over sand or clay. We set the layer thickness H to 0 (no layer; homogeneous background medium), 100, 200, 400, 600, 800, and 1,000 m, and the frequency f to 5 Hz. These thickness values, when normalized to the incoming P wavelength λ_0 of 1.16 km ($\sqrt{3}\, V_{S0}/f$), are 0, 0.17, 0.34, 0.52, 0.69, 0.86. The absolute value of the frequency f is not crucial in this study since the results are identical with respect to the normalized thickness, H/λ_0. For example, a simulation with f of 1 Hz and H of 1,000 m yields the same polarization angles as for 5 Hz and 200 m. In other words, the results obtained using a single f and multiple H values can be interpreted as those from a single H and multiple f values.

We use a conservative criterion for selecting polarization measurements with high linearity, which ensures that measurements are mainly derived from the first arriving direct wave. We find that a linearity threshold of 99.9% works well for selecting the direct wave, but the exact threshold level does not change the results significantly.

3.1. Dependence of Depth Sensitivity on Layer Thickness, Frequency, and Wave Speeds

For a given ray parameter, V_{S1}, and $V_{S0} > V_{S1}$, the measured P polarization angle decreases as H increases (Figure 1b). When $H = 0$, the medium is homogeneous with the background shear wave speed of V_{S0}, and the measured angle is identical to the predicted value based on V_{S0} and the ray parameter (equation (2)). For example, in the case where $x = 40$ km and $V_{S1} = 1.68$ km/s (0.5 of V_{S0}), the measured angle is 24.8° with nearly zero uncertainty, in agreement with the prediction. For H= 100 and 200 m, the angle decreases to 16.3 $\pm$ 1.5° and 13.4 $\pm$ 1.0°, respectively. When H is 400 m, the angle becomes 12.3 $\pm$ 0.5° which is the same as the predicted value based on a half space with a wave speed of 1.68 km/s (i.e., V_{S1}). Beyond 400 m, increasing H does not change the polarization significantly and the measurements reach a plateau.

The shear wave speed estimates exhibit similar patterns as the polarization measurements, that is, decreasing with increasing H and reaching a plateau at about $H = 400$ m in the case of $x = 40$ km and $V_{S1} = 1.68$ km/s (blue curve in Figure 1c). By examining how quickly the wave speed decreases, we can infer how the

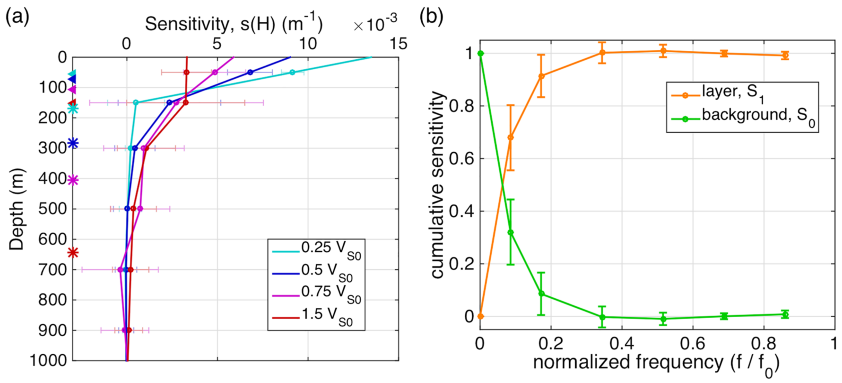

Figure 2. (a) Sensitivity $s(H)$ (equation (5)) calculated using the V_S measurements in Figure 1(c). Each line corresponds to the line with the same color in Figure 1(c). $H_{0.5}$ (triangles) and $H_{0.95}$ (asterisks) for different V_{S1} are marked using the same color scheme. (b) Frequency-dependent cumulative sensitivity of the P wave polarization to the background (S_0; green) and the layer (S_1; orange) at $x = 40$ km and V_{S1} of 0.5 V_{S0} (corresponding to blue lines in Figure 1b and 1c).

sensitivity changes over depth. If the sensitivity were constant over the depth range from the surface to about 400 m, then the wave speed would decrease linearly with H. However, the estimated speed decreases more steeply than linearly, that is, in a concave-up fashion, which indicates that the sensitivity decreases as depth increases. Therefore, the depth sensitivity of P wave polarization is maximum at the surface and decreases rapidly.

This is confirmed by the calculated depth sensitivity based on equation (5) (Figure 2a). For the case $x = 40$ km and $V_{S1} = 1.68$ km/s, the sensitivity decreases by about half for every 100 m in depth and reaches approximately zero at 500-m depth, a depth shallower than half of the incoming wavelength $\lambda_0 = 1.16$ km. Note that the 500-m depth differs from the depth at which the angle measurement reaches plateau, that is, 400 m, by 100 m, due to the crude discretization of depth H, that is, 200 m. The depth above which 95% of the sensitivity resides, $H_{0.95}$, is about 282 m, which indicates only about 5% sensitivity is attributed to the depth range 282 to 500 m. The depth above and below which half of the sensitivity resides, $H_{0.5}$, that is, the average depth that the P wave polarization is sensitive to, is about 74 m. It is considerably shallower than the incoming wavelength λ_0 of 1.16 km and P and S wavelengths within the layer, that is, $\sqrt{3}\,V_{S1}/f$ and V_{S1}/f, which are 582 and 336 m, respectively.

The observed dependence of P wave polarization on H also indicates its strong dependence on frequency content since the normalized thickness H/λ_0 can be interpreted as normalized frequency for a given medium with a fixed layer thickness H. The normalized thickness H/λ_0 is equivalent to a normalized frequency, that is, f/f_0, where $f_0 = \sqrt{3}\,V_{S0}/H$ is a reference frequency that is the reciprocal of the time it takes for a P wave to travel the layer at the speed of the background medium. Therefore, for a given medium, polarization and wave speed estimates are functions of frequency f (Figure 1b and 1c), making the depth sensitivity frequency dependent. Based on wave speed estimates at different normalized frequencies (Figure 1c), we obtain cumulative sensitivity to the layer S_1 (equation (4)) and the background medium S_0 (Figure 2b). At zero frequency, P wave polarization is only sensitive to the background, but as frequency increases, its sensitivity to the background diminishes rapidly, while increasing its sensitivity to the layer. In the case of $x = 40$ km and $V_{S1} = 0.5 \times V_{S0}$, frequencies higher than 0.34 times the reference frequency f_0 are primarily sensitive to the layer.

Shear wave speed of the layer V_{S1} is another important parameter for determining the depth sensitivity of P wave polarization. To explore the effect of V_{S1}, we focus on the case $x = 40$ km, that is, ray parameter of 7.1 s/°, which is within the typical range of teleseismic ray parameters, but the choice of ray parameter does not have a significant effect on the sensitivity (Text S1). We find that lower the V_{S1}, the wave speed estimate V_S^* converges to V_{S1}, faster, that is, at smaller H. For example, when V_{S1} is $0.25 \times V_{S0}$, that is, 0.84 km/s, the shear wave speed estimate V_S^* is 1.05 ± 0.16 km/s at H of 100 m, considerably closer to V_{S1}, than V_{S0} (Figure 1c). In contrast, when V_{S1} is as large as $1.5 \times V_{S0}$, V_S^* is still closer to V_{S0} than to V_{S1} at H of 100 m. Only when H becomes 800 m, does V_S^* reach V_{S1}. The effect of V_{S1} is also evident in the corresponding sensitivity curves

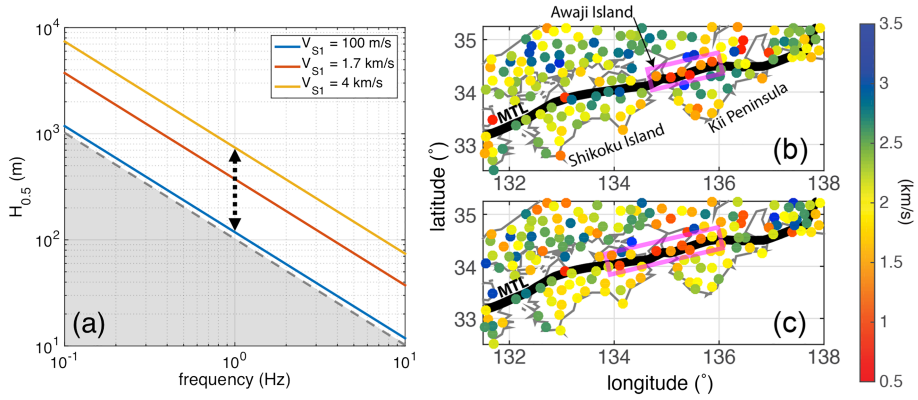

Figure 3. (a) The average depth $H_{0.5}$, at which *P* wave polarization is sensitive to, as a function of frequency for a fixed V_{S0} of 3.36 km/s and different V_{S1} values of 100 m/s (blue solid line), 1.7 km/s (orange solid line), and 4 km/s (yellow solid line). The gray dashed line marks the limit of $V_{S1} = 0$, and the shaded area below the line is not considered. The average depths that 1-Hz data with V_{S1} ranging from 100 m/s to 4 km/s are sensitive to are marked with black dotted arrow. (b) Vs estimate at each site (colored circle) in Japan based on body-wave polarization. Same as Figure 6a in Park and Ishii (2018), except for the plotting area focuses on Shikoku Island, Awaji Island, and Kii Peninsula. The Median Tectonic Line shown in solid black line and the magenta box highlights the zone with low wave speeds. (c) Same as (b) except that Vs is based on borehole measurements most of which are at 100-m depth.

(Figure 2a). As V_{S1} decreases, sensitivity decreases more steeply with respect to depth and $H_{0.5}$ and $H_{0.95}$ decrease, that is, polarization is sensitive to shallower structure. This is expected since lower wave speed implies a shorter wavelength; a more comprehensive discussion of this is in section 3.2.

3.2. Empirical Scaling of Depth Sensitivity With Wavelength

In order to investigate how the depth sensitivity scales with the two relevant wavelengths of the background and the layer, the sensitivity curves have been plotted against depths that are normalized with different reference length scales, denoted λ_{norm}: λ_{S0} and λ_{S1} (*S* wavelengths within the half space and the layer, that is, V_{S0}/f and V_{S1}/f, respectively), and a combination of the two, that is, $X\,\lambda_{S0}+(1-X)\,\lambda_{S1}$ where $0 < X < 1$ (Figure S3). We find that normalization with a length scale based on $X = 0.16$ results in sensitivity curves that are most consistent with each other. The normalizing wavelength $\lambda_{norm} = 0.16\,\lambda_{S0} + 0.84\,\lambda_{S1}$ yields the $H_{0.5}$ and $H_{0.95}$ values of different sensitivity curves that coincide with each other the best, i.e., minimizes the sum of the variances of $H_{0.5}$ and $H_{0.95}$ (Figure S3e). The fractions 16% and 84% suggest that the depth sensitivity of *P* wave polarization is controlled by both layer and background structure, that is, V_{S0} and V_{S1}, but is more influenced by the layer structure V_{S1}.

Based on the normalization using $\lambda_{norm} = 0.16\,\lambda_{S0} + 0.84\,\lambda_{S1}$, we can estimate $H_{0.5}$ and $H_{0.95}$, $H_{0.5} = 0.19\,\lambda_{norm}$ and $H_{0.95} = 0.71\,\lambda_{norm}$. The fact that both $H_{0.5}$ and $H_{0.95}$ are fractions of λ_{norm} demonstrates that *P* wave polarization is sensitive to a depth range that is significantly shallower than not only *P* wavelengths but also *S* wavelengths. Rewriting $H_{0.5}$ in terms of wave speeds and frequency yields an empirical relationship

$$H_{0.5} = 0.19 \times \frac{0.16\,V_{S0} + 0.84\,V_{S1}}{f}. \quad (6)$$

The average depth $H_{0.5}$ that *P* wave polarization is sensitive to is inversely proportional to frequency, while having positive linear relationships with shear wave speeds. For V_{S0} of 3.36 km/s (Kennett & Engdahl, 1991), $H_{0.5}$ can be calculated with respect to frequency at different values of V_{S1} (Figure 3a). For a given site with fixed wave speeds V_{S1}, the higher the frequency *f*, the shallower the sensitive depth range becomes. Furthermore, polarizations observed at a site with high V_{S1} samples deeper than one at a site with low V_{S1} even if the observations are made at the same frequency.

3.3. Application to Observed *P* wave Polarizations in Japan

Based on our analysis on the depth sensitivity of *P* wave polarization, we can revisit the observed polarizations and inferred wave speeds in Park and Ishii (2018) to understand the depth sensitivity. The average

depth $H_{0.5}$ can be estimated under the assumption that V_{S1} can be approximated by the estimated shear wave speeds in the range 0.1-4 km/s and that the shear wave estimates are mainly constrained by *P* wave polarizations. For the dominant frequency of the data, that is, 1 Hz, $H_{0.5}$ ranges from about 118 to 741 m. For an average V_{S1} of 1.7 km/s, $H_{0.5}$ is 373 m. These sensitivity depths are deeper than the 100-m boreholes at which most of the benchmark wave speeds were measured, implying that the wave speed estimates are for structure at depths not reached by drilling. The fact that polarization-based wave speed estimates are consistent with the borehole measurements suggests that the structure at 100-m depth generally extends to 373 m on average and to 741 m for fast sites and lateral variations in the overall structure of Japan at 100 m also persists to deeper depths (Figure 3b and 3c). One of the interesting examples is the distinct low-wave-speed feature along a part of the Median Tectonic Line, a major fault zone in Japan (e.g., Tsutsumi & Okada, 1996). A ~90-km long segment of this linear feature running through the west of the Kii peninsula and Awaji Island is evident in both polarization-based and borehole wave speeds, with the shear wave speeds ranging from 0.1 to 1.4 km/s. It indicates that this segment of the Median Tectonic Line is weaker than the surrounding medium, and the weak zone extends to ~330 m based on equation (6). For the borehole measurements, the feature also continues to the west for about 30 km into the Shikoku Island, which is not the case for the polarization-based results. These differences suggest that the weak zone associated with this segment does not penetrate much deeper than 100 m. Thus, the Median Tectonic Line exhibits spatially variable weaknesses in structure, with the 90-km segment on the west side of the Kii peninsula and Awaji Island being the weakest part.

For the same range of V_{S1} from 0.1 to 4 km/s, expanding the analysis into different frequencies will help constrain structure at considerably different depths. Lowering the frequency to 0.1 Hz makes $H_{0.5}$ as deep as 1 to 7 km, which is within the upper crust (Kennett & Engdahl, 1991). High frequency observations at 5–10 Hz, which can be acquired by local events, short-period sensors, or filtering broadband data, will be sensitive to depth ranges of 12 to 148 m.

4. Conclusions

We have investigated the depth sensitivity of *P* wave polarization based on simulations for a layer over a half space. The sensitivity peaks at the surface and decreases rapidly. The depth above which 95% of the sensitivity resides is shallower than not only the incoming *P* wavelength but the *S* wavelength in the layer. Furthermore, the average depth that the *P* wave polarization is sensitive to is only about 20% of the relevant shear wavelength. The results reveal a shallow sub-wavelength sensitivity of *P* wave polarization distinctly different than that of conventional travel times which is distributed along the whole ray path.

We find that the depth sensitivity of *P* wave polarization is characterized by a length scale that is mainly controlled by frequency and shear wave speed in the layer. The higher the frequency, the shallower the sensitivity, while the higher the wave speed, the deeper the sensitivity. The results provide quantitative estimates of the sampling depths of *P* wave polarization, which ranges from 100 to several hundreds of meters for 1-Hz data. Applying the results to observations in Japan illuminates structure at about 120 to 750 m, including a distinctive weak zone along the Median Tectonic Line in the Kii peninsula and Awaji Island. For future studies, high frequency data, that is, 5 to 10 Hz, can be utilized to investigate seismic structure in the top 10 to hundred meters and low frequency data at 0.1 Hz and below can be used to study the upper crust and deeper structure. Furthermore, extending our analyses to general models beyond a layer over half space, for example, with linearly increasing wave speeds in the layer or multilayer models, and combining the analysis of *S* wave polarization will help illuminate local 1-D structure at shallow depths.

Acknowledgments
The authors thank the editor Jeroen Ritsema and two anonymous reviewers for helpful comments. S.P. thanks Hiroo Kanamori for valuable discussion about the Median Tectonic Line. The early phase of this work was supported by NSF grant EAR-1735960. S. P. was also supported by the Caltech Texaco Postdoctoral Fellowship. The waveform simulation code was obtained from QUEST (http://www.quest-itn.org/library/software/reflectivity-method.html).

References

Abercrombie, R. E. (1997). Near-surface attenuation and site effects from comparison of surface and deep borehole recordings. *Bulletin of the Seismological Society of America*, *87*(3), 731–744.

Berbellini, A., Morelli, A., & Ferreira, A. M. G. (2017). Crustal structure of northern Italy from the ellipticity of Rayleigh waves. *Physics of the Earth and Planetary Interiors*, *265*, 1–14. https://doi.org/10.1016/J.PEPI.2016.12.005

Boore, D. M., Joyner, W. B., & Fumal, T. E. (1997). Equations for estimating horizontal response spectra and peak acceleration from western North American earthquakes: A summary of recent work. *Seismological Research Letters*, *68*(1), 128–153. https://doi.org/10.1785/gssrl.68.1.128

Borcherdt, R. D., & Glassmoyer, G. (1992). On the characteristics of local geology and their influence on ground motions generated by the Loma Prieta earthquake in the San Francisco Bay region, California. *Bulletin of the Seismological Society of America*, *82*(2), 603–641.

Choukroune, P. (1989). The ECORS Pyrenean deep seismic profile reflection data and the overall structure of an orogenic belt. *Tectonics*, *8*(1), 23–39. https://doi.org/10.1029/TC008i001p00023

Dahlen, F. A., Hung, S. H., & Nolet, G. (2000). Fréchet kernels for finite-frequency traveltimes-I. Theory. *Geophysical Journal International*, *141*(1), 157–174. https://doi.org/10.1046/j.1365-246X.2000.00070.x

Hannemann, K., Krüger, F., Dahm, T., & Lange, D. (2016). Oceanic lithospheric *S*-wave velocities from the analysis of *P*-wave polarization at the ocean floor. *Geophysical Journal International*, *207*(3), 1796–1817. https://doi.org/10.1093/gji/ggw342

Hu, G., Menke, W., & Powell, C. (1994). Polarization tomography for *P* wave velocity structure in southern California. *Journal of Geophysical Research*, *99*(B8), 15,245–15,256. https://doi.org/10.1029/93JB01572

Kennett, B. L. N. (1986). Seismic wave propagation in stratified media. *Geophysical Journal of the Royal Astronomical Society*, *86*(1), 219–220 . https://doi.org/10.1111/j.1365-246X.1986.tb01087.x

Kennett, B. L. N., & Engdahl, E. R. (1991). Traveltimes for global earthquake location and phase identification. *Geophysical Journal International*, *105*(2), 429–465. https://doi.org/10.1111/j.1365-246X.1991.tb06724.x

Kruger, F. (1994). Sediment structure at GRF from polarization analysis of *P* waves of nuclear explosions. *Bulletin of the Seismological Society of America*, *84*(1), 149–170.

Laske, G., & Masters, G. (1996). Constraints on global phase velocity maps from long-period polarization data. *Journal of Geophysical Research*, *101*(B7), 16,059–16,075. https://doi.org/10.1029/96JB00526

Levander, A., Hobbs, R. W., Smith, S. K., England, R. W., Snyder, D. B., & Holliger, K. (1994). The crust as a heterogeneous "optical" medium, or "crocodiles in the mist". *Tectonophysics*, *232*(1–4), 281–297.

Lin, F.-C., Tsai, V. C., & Schmandt, B. (2014). 3-D crustal structure of the western United States: Application of Rayleigh-wave ellipticity extracted from noise cross-correlations. *Geophysical Journal International*, *198*(2), 656–670. https://doi.org/10.1093/gji/ggu160

Mitchell, B. J., & Yu, G. (1980). Surface wave dispersion, regionalized velocity models, and anisotropy of the Pacific crust and upper mantle. *Geophysical Journal International*, *63*(2), 497–514. https://doi.org/10.1111/j.1365-246X.1980.tb02634.x

Park, S., & Ishii, M. (2018). Near-surface compressional and shear wave speeds constrained by body-wave polarization analysis. *Geophysical Journal International*, *213*(3), 1559–1571. https://doi.org/10.1093/gji/ggy072

Parsekian, A. D., Singha, K., Minsley, B. J., Holbrook, W. S., & Slater, L. (2015). Multiscale geophysical imaging of the critical zone. *Reviews of Geophysics*, *53*, 1–26. https://doi.org/10.1002/2014RG000465

Pearson, K. (1901). Principal components analysis. *The London, Edinburgh and Dublin Philosophical Magazine and Journal*, *6*(2), 566.

Phinney, R. A. (1964). Structure of the Earth's crust from spectral behavior of long-period body waves. *Journal of Geophysical Research*, *69*(14), 2997–3017. https://doi.org/10.1029/JZ069i014p02997

Shearer, P., & Orcutt, J. (1987). Surface and near-surface effects on seismic waves—Theory and borehole seismometer results. *Bulletin of the Seismological Society of America*, *77*(4), 1168–1196. Retrieved from. http://www.bssaonline.org/content/77/4/1168.short

Svenningsen, L., & Jacobsen, B. H. (2007). Absolute *S*-velocity estimation from receiver functions. *Geophysical Journal International*, *170*(3), 1089–1094. https://doi.org/10.1111/j.1365-246X.2006.03505.x

Tanimoto, T., & Rivera, L. (2008). The ZH ratio method for long-period seismic data: Sensitivity kernels and observational techniques. *Geophysical Journal International*, *172*(1), 187–198. https://doi.org/10.1111/j.1365-246X.2007.03609.x

Tsutsumi, H., & Okada, A. (1996). Segmentation and Holocene surface faulting on the Median Tectonic Line, southwest Japan. *Journal of Geophysical Research*, *101*(B3), 5855–5871. https://doi.org/10.1029/95JB01913

Woodward, M. J. (1992). Wave-equation tomography. *Geophysics*, *57*(1), 15–26. https://doi.org/10.1190/1.1443179

Wu, R.-S., Xu, Z., & Li, X.-P. (1994). Heterogeneity spectrum and scale-anisotropy in the upper crust revealed by the German Continental Deep-Drilling (KTB) Holes. *Geophysical Research Letters*, *21*(10), 911–914. https://doi.org/10.1029/94GL00772